Object separation by polarimetric and spectral imagery fusion ☆

Y. Zhao [a], L. Zhang [b,*], D. Zhang [b], Q. Pan [a]

[a] College of Automation, Northwestern Polytechnical University, Xi'an, China
[b] Dept. of Computing, The Hong Kong Polytechnic University, Hong Kong, China

ARTICLE INFO

ABSTRACT

When light is reflected from object surface, its spectral characteristics will be affected by the surface's elemental composition, and its polarimetric characteristics will be governed by the surface's roughness and conductance. Polarimetric and multispectral imaging can provide complementary discriminative information in applications such as object separation. However, few methods have been proposed to fuse the information provided by polarimetric and multispectral imagery for better object separation results. Considering that the metal and dielectric materials, and the manmade objects and natural background have different polarimetric and multispectral features, in this paper we propose a simple yet powerful method for object separation by using the polarimetric and spectral characteristics of specular and diffuse reflected light. A polarimetric imagery fusion algorithm is first proposed based on the degree of linear polarization modulation to distinguish different objects. Then the spectral and polarimetric information, which can be extracted from the specular and diffuse reflected light, is fused by using the HSI color space mapping for more robust object separation. Experiments on real outdoor and indoor images are performed to evaluate the efficiency of the proposed scheme.

© 2009 Elsevier Inc. All rights reserved.

1. Introduction

The human visual system perceives scenes in terms of intensity and color in visual band of the electromagnetic spectrum. As a fundamental property of light, polarization is not available to the human visual system and it is ignored in most automated vision systems. However, the polarization of light can provide much new information, other than the intensity of light, for automated vision systems. Based on the Fresnel theory [15], polarization can reflect the object surface characteristics and it has been used for surface modeling [1], shape recovery [2,3] and reflectance analysis [4]. According to the principle that the backscatter in scatter media is partially polarized, polarimetric imaging can be used to remove degradation effects in underwater vision and acquire the scene structure (distances) information [5]. At the same time, polarization can significantly simplify some important visual tasks, which are too complicated to accomplish or even infeasible by using only intensity and color information, for instance, dielectric and metal discrimination, and quantitative separation of specular and diffuse reflection components, etc. [6–8].

A couple of polarimetry based dielectric and metal separation methods have been proposed [6–9]. Since specular reflection usually leads to polarized light, the image of an object through a polarizer will exhibit changing intensities of the specular component as the polarizer is rotated. If we assume that the diffuse reflection is uniform in the highlight area, i.e. the area where strong specular reflection exists, separation of the specular component and diffuse component is possible [6]. Umeyama and Godin [1] analyzed the diffuse and specular components of surface reflection and applied ICA (independent component analysis) to the images observed by a polarizer of different orientations to separate diffuse and specular components. Wolff [6] presented a *Fresnel reflectance model* to estimate *polarization Fresnel ratio* to discriminate metal and dielectric surfaces from specular reflection. In [11] Wolff et al. proposed a scheme to classify the solder metal and plastic dielectric by thresholding the ratio I_{max}/I_{min}, where I_{max} is the intensity when polarizer orientation is aligned parallel to the orientation of the linear polarized component, and I_{min} is the intensity when polarizer orientation is aligned perpendicular to the orientation of the linear polarized component.

The other type of object separation approaches exploits the spectra of the reflected light. Because metal and dielectric surfaces are composed of different materials, their reflective spectra are different. Therefore, the surfaces can be distinguished using the spectra of the reflected light. Tominaga and Okamoto [24] proposed a reflectance based method to distinguish plastics and metals but this method needs two illumination directions. Nayar et al. [12]

proposed an object separation method by using the spectral information in Red, Green and Blue bands and the polarization properties of the reflected light simultaneously. This method can separate the specular and diffuse components without assuming the uniformity of the diffuse reflection.

The above object separation methods use only a rotating polarizer (or multiple filters) and thresholding operations. They are simple and effective, however, only in indoor and ideal lighting situations. For outdoor scenes, the lighting conditions are much more complex and the above methods will not work well. Nonetheless, in computer vision applications, outdoor scene understanding is very important. It is necessary to develop new polarimetric techniques to effectively separate the different objects in outdoor scenes.

Despite the fact that both polarimetric and spectra information can be used to discriminate objects, few methods have been reported to exploit the two types of characteristics simultaneously for better results. In this paper, a novel object separation scheme is presented by fusing the polarimetric and multispectral imagery. We first propose a polarimetric imagery fusion algorithm to distinguish different objects based on the degree of linear polarization modulation. We then fuse the spectral and polarimetric information by using HSI color space mapping for better and more robust object separation results. The proposed scheme is robust to illumination conditions. It can effectively separate dielectric and metal objects, and it is also able to distinguish manmade objects from natural background based their different surface roughness.

The rest of the paper is organized as follows. Section 2 introduces the concepts of polarization and spectra. Section 3 describes the spectral and polarization imagery fusion algorithm in detail. Section 4 presents experimental results and Section 5 concludes.

2. Polarization and spectra

According to the refraction index $\eta = n - ik$ of materials, most object surfaces can be classified as one of the two broad material classes: metals ($n \neq 0$ and $k \neq 0$) or dielectrics ($n \neq 0$ and $k \approx 0$). Metals have low electrical resistivity due to the free movement of electrons between atoms and thus they are very good conductors. Comparatively, dielectric materials are very poor conductors of electricity. Since all light is electromagnetic radiation, the differences in the electrical characteristics between metals and dielectrics lead to differences in how light reflects off these materials. Dielectric surfaces partially polarize light upon specular reflection for most specular angles of incidence [11,14–15]. At the same time, the refraction index η is a function of wavelength, which means that the intensity of reflected light will vary accompany with the variation of wavelength. This section introduces the basic concepts of polarimetry and spectrometry. For more information, please refer to [10,15,16].

2.1. The Fresnel reflectance coefficients for dielectrics and metals

The Fresnel equations give the ratios of the reflected wave amplitude to the incident wave amplitude for incident light that is linearly polarized perpendicular to, or parallel to, the plane of specular incidence [15]. These ratios depend upon the angle of incidence and the refractive index of the reflecting medium. Since the incident light can always be resolved into components perpendicular to and parallel to the plane of incidence, the Fresnel equations are applicable to all incident polarization states.

The amplitude reflection coefficient for light polarized parallel to the plane of incidence at a boundary between two media is given by

$$r_{\parallel}(n_i, \eta, \theta_i, \theta_r) = \frac{E_{r\parallel}(n_i, \eta, \theta_i, \theta_r)}{E_{i\parallel}} = \frac{\eta \cos\theta_i - n_i \cos\theta_r}{\eta \cos\theta_i + n_i \cos\theta_r}. \tag{1}$$

For light polarized perpendicular to the plane of incidence, there is

$$r_{\perp}(n_i, \eta, \theta_i, \theta_r) = \frac{E_{r\perp}(n_i, \eta, \theta_i, \theta_r)}{E_{i\perp}} = \frac{n_i \cos\theta_i - \eta \cos\theta_r}{n_i \cos\theta_i + \eta \cos\theta_r}, \tag{2}$$

where θ_i and θ_r are the angles of incidence and refraction, respectively. $E_{\perp}$ is the polarization component perpendicular to the specular plane and $E_{\parallel}$ is the polarization component parallel to the specular plane. The relation between θ_i and θ_r is determined by the *Snell's* law:

$$n_i \sin\theta_i = c\sqrt{\left(\varepsilon - i\frac{\sigma}{\omega}\right)\mu}\sin\theta_r = (n - ik)\sin\theta_r = \eta\sin\theta_r, \tag{3}$$

where $n_i = 1$ is the refractive index of air, ε is the permittivity of material, ω is the frequency of light, σ is the electrical conductivity of material surface, μ is the permeability of material surface, n is the simple index of refraction, and term k is called the coefficient of extinction.

2.2. Polarimetry

Reflection of light from surfaces can be classified into two broad categories: diffuse and specular. The measured intensity of light is composed of the two parts and the polarized light can be described by three elements: total intensity (*Int*), the degree of polarization (*DoLP*) and the phase of polarization (*Orient*). If we assume that the diffuse component is unpolarized, the three parameters can be described as follows.

First the total intensity can be defined as

$$Int(\lambda, \eta, \theta_i) = I_{min}(\lambda, \eta, \theta_i) + I_{max}(\lambda, \eta, \theta_i), \tag{4}$$

where

$$I_{max}(\lambda, \eta, \theta_i) = \frac{1}{2}I_d + \frac{r_{\perp}^2(\lambda, \eta, \theta_i)}{r_{\perp}^2(\lambda, \eta, \theta_i) + r_{\parallel}^2(\lambda, \eta, \theta_i)}I_s, \tag{5}$$

$$I_{min}(\lambda, \eta, \theta_i) = \frac{1}{2}I_d + \frac{r_{\parallel}^2(\lambda, \eta, \theta_i)}{r_{\perp}^2(\lambda, \eta, \theta_i) + r_{\parallel}^2(\lambda, \eta, \theta_i)}I_s. \tag{6}$$

The degree of polarization is defined as

$$\begin{aligned} DoLP(\lambda, \eta, \theta_i) &= \frac{I_{max}(\lambda, \eta, \theta_i) - I_{min}(\lambda, \eta, \theta_i)}{I_{max}(\lambda, \eta, \theta_i) + I_{min}(\lambda, \eta, \theta_i)} \\ &= \frac{r_{\perp}^2(\lambda, \eta, \theta_i) - r_{\parallel}^2(\lambda, \eta, \theta_i)}{r_{\perp}^2(\lambda, \eta, \theta_i) + r_{\parallel}^2(\lambda, \eta, \theta_i)} \cdot \frac{1}{1 + \frac{I_d}{I_s}} \\ &= \frac{r_{\perp}^2(\lambda, \eta, \theta_i) - r_{\parallel}^2(\lambda, \eta, \theta_i)}{r_{\perp}^2(\lambda, \eta, \theta_i) + r_{\parallel}^2(\lambda, \eta, \theta_i)} \cdot \frac{1}{1 + DSratio} \end{aligned} \tag{7}$$

where $DSratio = I_d/I_s$ is the ratio between diffuse and specular components of reflection. Fig. 1(a) shows the *DoLP* for poorly conducting glass ($n = 1.89$), intermediately conducting iron ($n - ik = 1.51 - 1.63i$, $\lambda = 0.589\,\mu m$) and highly conducting copper ($n - ik = 0.82 - i5.99$, $\lambda = 0.65\,\mu m$), illustrating the *DoLP*'s variation along incident angle and refraction index. Fig. 1(b) shows the *DoLP*'s variation along incident angle and *DSration*, illustrating that the ratio between diffuse and specular components will affect the value of *DoLP* but will not change the difference of *DoLP* among different materials.

The phase of polarization is defined as

$$Orient = \frac{1}{2}\arctan(\cos(\delta).\tan(2\alpha)), \tag{8}$$

where $\tan\alpha = E_{oy}/E_{ox}$, δ is the relative phase shift, and E_{ox} and E_{oy} are the maximum amplitudes in the x and y directions. In Fig. 1(a), when the specular angle of incidence is greater than 75° or near horizontal incidence, it is difficult or even impossible to distinguish
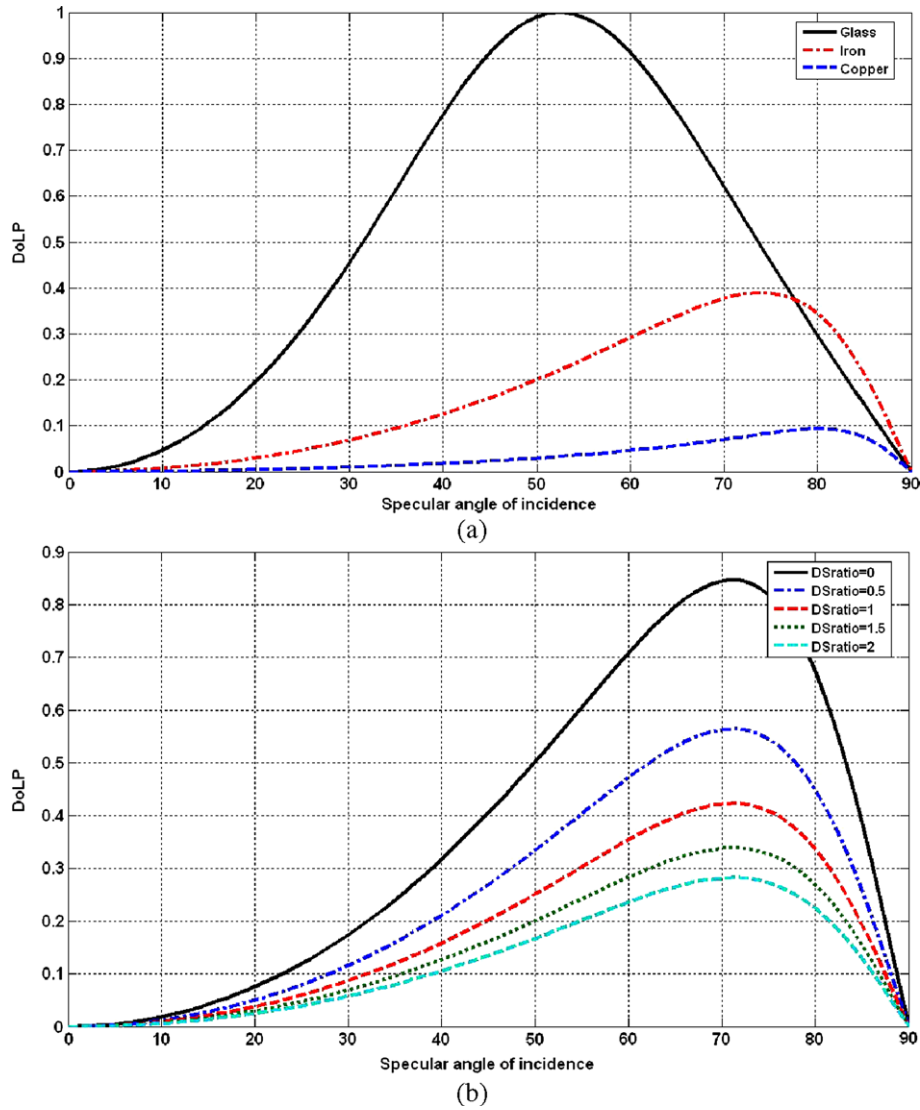
Fig. 1. (a) The degree of linear polarization vs. angle of incidence for different materials; (b) the degree of linear polarization vs. angle of incidence for specular reflection for different *DSratio* (iron).

dielectrics and metals. *Orient* depends on the relative phase shift δ and $\alpha = \arctan(E_{oy}/E_{ox})$. Different α will cause different orient changes between dielectrics and metals. Fig. 2 shows the *Orient*'s variation along incident angle and the relative phase shift δ and α.

From Figs. 1 and 2, it can be seen that *DoLP* and *Orient* have their own advantages and disadvantages in discriminating dielectrics and metals. If the *DoLP* and *Orient* information can be fused, better object discriminate performance can be expected.
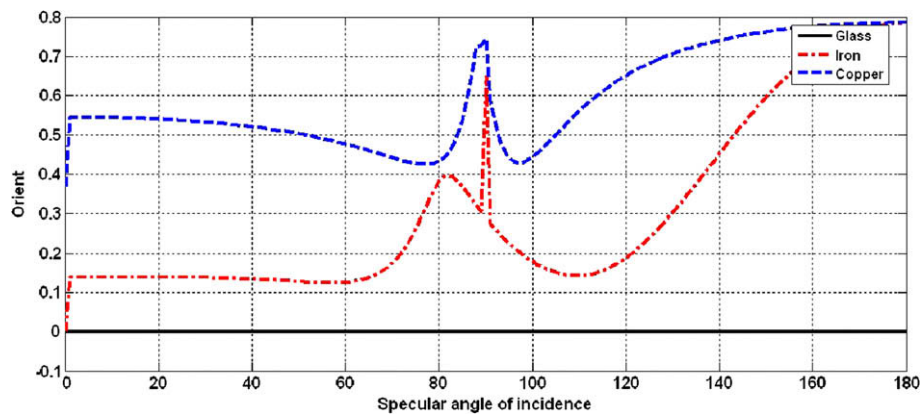

Fig. 2. The *Orient* vs. angle of incidence for different materials.

2.3. Spectral reflectance

Spectral reflectance is the ratio of energy reflected from a surface in a given waveband to the energy incident in that waveband, which depends on the material composition [17,24]. According to (1) and (2), the spectral reflectance at wavelength λ can be represented as

$$r(n_i, \eta, \theta_i, \theta_r, \lambda) = \frac{E_r(n_i, \eta, \theta_i, \theta_r, \lambda)}{E_i(\lambda)} \tag{9}$$

Spectral reflectance can be divided into two parts: specular reflectance and diffuse reflectance. Reflection from homogeneous materials like metals is based mostly on the specular reflection. For inhomogeneous materials like plastics and paints, the diffuse reflectance component is meaningful [24]. From (1), (2) and (9), it can be concluded that spectral reflectance reflects the variation of ratios of energy at different wavelengths, while polarization reflects the variation of ratios of energy at different vibration directions.

In many applications measuring up to several different bands, including the near-infrared (near-IR), will provide much more discrimination information than by using a tri-chromatic (RGB) image. The spectral reflectance $r(n_i, \eta, \theta_i, \theta_r, \lambda)$ can be used to discriminate the material exclusively, but it requires a huge volume of datasets to acquire the scene's spectral reflectance and this cannot be performed in real time. In many practical situations, by carefully selecting spectral bands, multispectral imaging will perform as well as hyperspectral imaging with the same spatial resolution.

3. Spectral and polarimetric imagery fusion

Polarization is a more general physical characteristic of light than intensity. It can carry additional information of the object surface, thus providing a richer description of the scene [6,11]. Meanwhile, different polarimetric parameters, such as *Int*, *DoLP* and *Orient*, reflect different characteristics of the interested scene and those characteristics can be fused for a better description of the object. In Section 3.1, an algorithm will be proposed to fuse the *Int*, *DoLP* and *Orient* information to distinguish different objects. Since polarimetric and multispectral imagery can provide complementary information for the scene, if they can be integrated, better material and object discrimination performance can be expected. To this end, in Section 3.2 a polarimetric and multispectral imagery fusion algorithm will be presented.

3.1. Polarization image fusion based on DoLP modulation

Fig. 3 shows an example of the polarimetric components, i.e. *Int*, *DoLP* and *Orient*, of an outdoor scene, which is composed of cars, concrete road and plants (tree, grass and shrub). The whole scene

can be divided into two groups: manmade objects (cars and road) and natural background (plants).

From Section 2 and Fig. 3, it can be seen that for metals the reflected light has a small value of *DoLP*, while for dielectrics the reflected light has a large value of *DoLP*. For rough surface the reflected light has a small value of *DoLP*, while for smooth surface the reflected light has a large value of *DoLP*. Overall, in remote sensing, the surface of manmade object is usually regarded as a smooth surface and has relatively large values of *DoLP*, and the surface of natural background is regarded as a rough surface and has relatively small values of *DoLP* [7]. This can also be seen in the *DoLP* image in Fig. 3, where the manmade objects (car and concrete road) have higher *DoLP* magnitudes than the natural background. Therefore, when the interested scene contains metal/dielectric or manmade/natural objects, the diversity of its *DoLP* component can be used to modulate the acquired image to enhance the contrast of those different objects.

A *DoLP* modulation coefficient can be defined to stretch the contrast and hence the separability of metal/dielectric or manmade/natural objects in polarimetric images. The modulation function should be continuous in the field of *DoLP* and should be monotonically increasing with *DoLP*. The logarithmic function is a natural choice for this purpose as pointed out by Shannon [18]. We define the *DoLP* modulation coefficient M_{DoLP} as follows:

$$M_{DoLP} = DoLP \cdot log(1 + DoLP) \tag{10}$$

Fig. 4 shows the variation of *DoLP* modulation coefficient along incident angle and refraction index. By comparing Fig. 1 with Fig. 4, we see that the difference between dielectrics and metals is enhanced by the *DoLP* modulation coefficient, especially along those incidence angles by which *DoLP* cannot distinguish dielectrics from metals.

According to the relationship between specular angle of incidence and the orient of polarization as shown in Fig. 2, the *Orient* varies very slowly in a local region of smooth surface but quickly for rough surface. To make the variation more obvious between rough and smooth surface, a local root mean square is calculated:

$$\overline{Orient} = \sqrt{\frac{M'N'}{\sum_{x=1}^{M'}\sum_{y=1}^{N'}(Orient(x,y) - \mu)^2}}, \tag{11}$$

where μ is the mean in a local region $M' \times N'$. In image $\overline{Orient}$, the pixel values in smooth regions are higher that those in rough regions.

The *DoLP* image can reflect materials' smoothness and conductance, and the image $\overline{Orient}$ can reflect surface smoothness, as can be seen in Fig. 3. Both the two components, however, contain little texture information of the objects. Fortunately, the *Int* image contains abundant texture information. If the *Int* image can be fused with the *DoLP* and $\overline{Orient}$ images, an image with better contrast and more detailed textures can be obtained. We propose here a false color mapping [13,19] and *DoLP* modulation based polarimet-
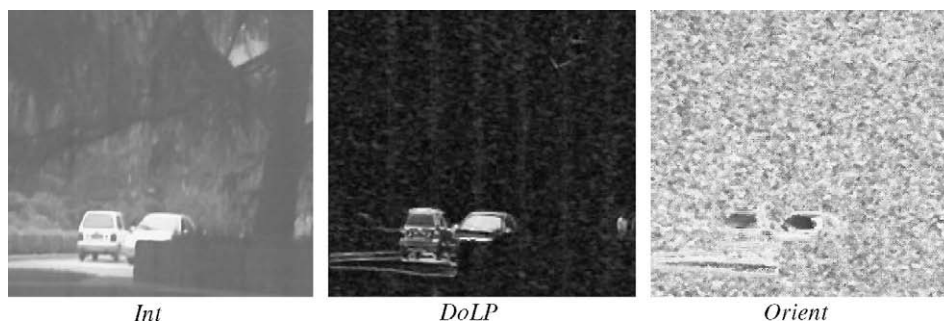

| *Int* | *DoLP* | *Orient* |

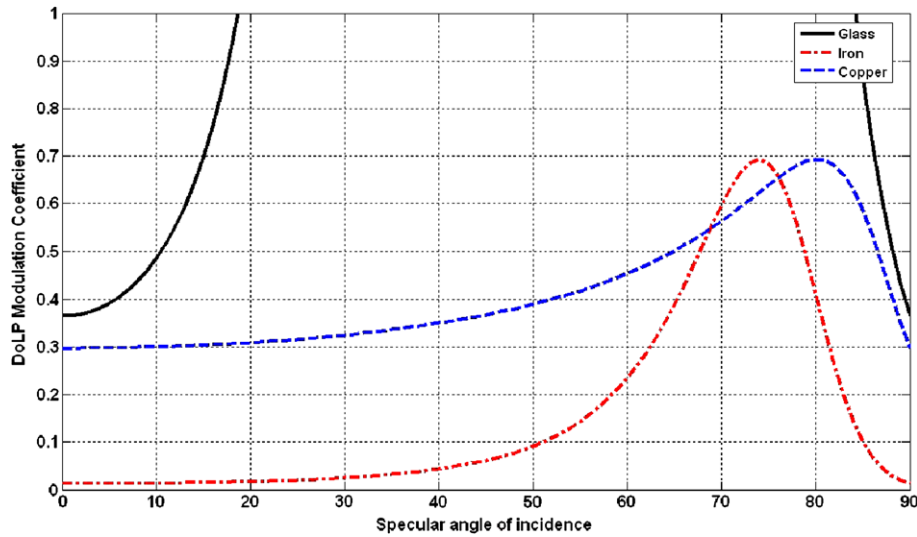**Fig. 3.** The polarimetric components, *Int*, *DoLP* and *Orient*, of an outdoor scene.

Fig. 4. The *DoLP* modulation coefficient vs. angle of incidence for different materials.

ric imagery fusion method to exploit the information from all the *Int*, *DoLP* and $\overline{Orient}$ images. It integrates the texture information of high spatial resolution *Int* image with the polarimetric information from low spatial resolution *DoLP* and $\overline{Orient}$ images to achieve better discriminability of metals and dielectrics, and manmade objects and natural background. The fusion process is described detailedly in the following Algorithm 1.

Algorithm 1

(1) Preprocess the *Int*, *DoLP* and $\overline{Orient}$ images, including image denoising and normalization.
(2) Find the common information among *Int*, *DoLP* and $\overline{Orient}$:

$$Co = Int \cap DoLP \cap \overline{Orient}, \tag{12}$$

where $A \cap B(i,j) = minA(i,j), B(i,j)$ (*A* and *B* represent digital images, and (i,j) represents the pixel coordinate).

(3) Calculate the unique part in each image:

$$\begin{cases} DoLP^* = DoLP - Co, \\ Orient^* = \overline{Orient} - Co, \\ Int^* = Int - Co. \end{cases} \tag{13}$$

The pairwise subtraction of multi-band images can be used to enhance the difference between them. In formula (13), through subtraction of the common component, the unique information will be enhanced in each image.

(4) Adjust the images by using the unique components:

$$\begin{cases} DoLP^{**} = DoLP - Orient^* - Int^*, \\ Orient^{**} = \overline{Orient} - DoLP^* - Int^*, \\ Int^{**} = Int - DoLP^* - Orient^*. \end{cases} \tag{14}$$

The unique components calculated by (12) are subtracted from the original image of other modalities. This step serves to enhance the representation of each modality's specific details in the final fused result.

(5) $F = RGB (Int^{**}, DoLP^{**}, Orient^{**})$

By transforming the Int^{**}, $DoLP^{**}$ and $Orient^{**}$ images into RGB space, the information contained in *Int*, *DoLP* and *Orient* images is combined in image *F*.

(6) Modulate the fused false color image *F* with the normalized *DoLP* modulation coefficient to get the final fused image:

$$Fusion = M_{\overline{DoLP}} \cdot F. \tag{15}$$

This step will stretch the contrast between metal and dielectric objects in final fused image *Fusion*.

In Algorithm 1, the three polarimetric image components (*Int*, *DoLP* and $\overline{Orient}$) are viewed as three different sensor modalities and fused through false color mapping. Fig. 5(b) shows the fusion result of the *Int*, *DoLP* and $\overline{Orient}$ images in Fig. 3 by using the proposed Algorithm 1. For comparison, Fig. 5(a) shows the image by using the I_{max}/I_{min} method, which was proposed by Wolff and Mancini [11]. We can see that it is much easier to separate the manmade objects (the car and concrete road, which are represented in red color in Fig. 5(b)) by using the proposed method. In Fig. 5(a), the intensities of the concrete road and part of the car are almost the same as those of the natural background by using the I_{max}/I_{min} method.

However, from Fig. 5(b) we can still see some limitations of Algorithm 1. Part of the car and part of the concrete road are mistakenly regarded as the natural background. The main reason is that the *DoLP* and *Orient* images of these regions are the mixture of manmade objects and the surrounding background. Thus, it is difficult to distinguish the desired objects in these regions by using only the polarimetric information. This is an inherited shortcoming of polarimetric imaging.

3.2. Spectral and polarimetric imagery fusion through false color mapping

The difficulty of polarimetric imaging mentioned above can be overcome by combining with multispectral imaging. Polarization is orthogonal to wavelength and hence polarimetric imaging and multispectral imaging are complementary. By exploiting more information about the scene of interested, better identification performance can be expected [20]. If we can find a way to fuse multispectral and polarimetric imagery, better object discrimination result can be obtained.

Wolff [6] proposed a scheme, which maps an image obtained from partially polarized light onto an image that is encoded using the HSI color scheme. It establishes a proper relationship between polarimetric and spectral information. Fig. 6 illustrates the mapping function.
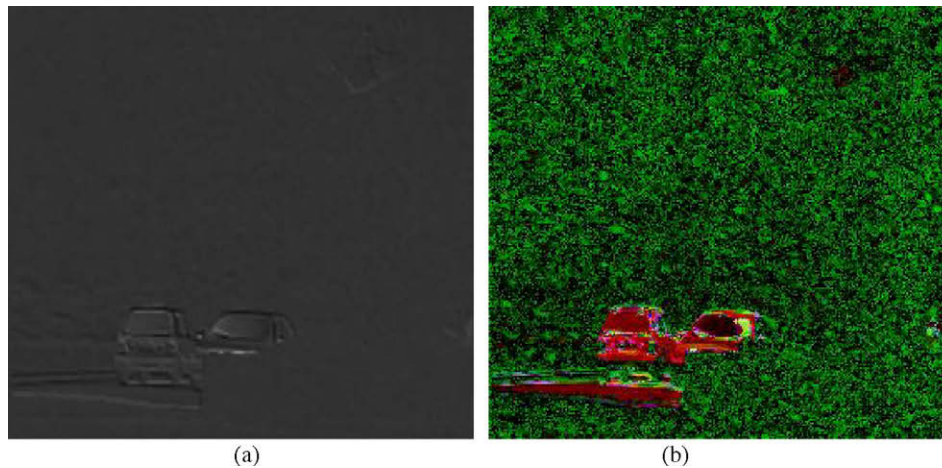
Fig. 5. Fused image by using (a) the I_{max}/I_{min} method and (b) the proposed Algorithm 1.
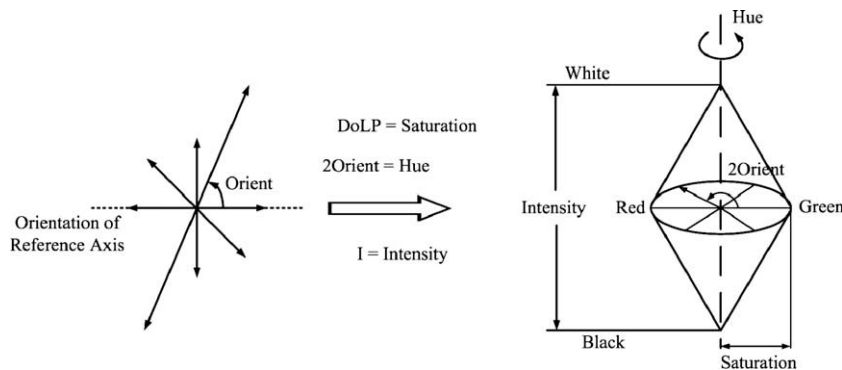

Fig. 6. HSI representation of partially linearized polarization images.

In Algorithm 1, through integrating and modulating the unique information of *Int, DoLP* and *Orient*, we have exploited the polarimetric information to separate different objects. With the mapping scheme in Fig. 6 and the characteristics of multispectral imagery, here we propose a false color mapping based multispectral and polarimetric imagery fusion algorithm as follows.

Algorithm 2

(1) Transform the multispectral image into the HSI color space.

Before the transformation, the multispectral images are registered and normalized. Then we partition the multispectral bands into three parts, and name them the R band set, G band set and B band set, respectively, based on their wavelengths. For each of the R, G and B band sets, we use the principal component analysis (PCA) to fuse the images in that set into one image, i.e. extracting the most significant component and taking it as the R, G or B output image. Finally, the obtained RGB color image is transformed into the HIS color space and we have the *Intensity*, *Saturation* and *Hue* components of the multispectral imagery.

(2) Map the polarimetric image into HSI color space based on Fig. 6.

Based on Fig. 6, the polarimetric *Int* image is taken as the *Intensity* component; the *DoLP* image is taken as the *Saturation* component; and the *Orient* image is mapped to the *Hue* component as $2^*Orient\mathit{l} = Hue$, respectively.

(3) Fuse the polarimetric *Int* image with the multispectral *Intensity* component to get a new polarimetric image (*NPI*).

As the polarimetric *Int* image and the multispectral *Intensity* component contain most details of the scene, wavelet based image fusion [21–23] is a good choice. By using wavelet based image fusion, the edges in multispectral and polarimetric images can be well preserved without introducing much error in the fused image. Meanwhile, we are interested in region features rather than pixel features in the image and the feature information should be incorporated into the fusion process. With the above considerations, we used the wavelet region based image fusion method [21,23,25] in this paper, which use regions to represent image features and determine the weighting coefficients. It has been reported that the region based image fusion is more robust to small registration errors than pixel based fusion [21].

(4) Fuse the polarimetric *DoLP* image with the multispectral *Saturation* component for a new *DoLP* image (*NDoLPI*).

There is little detailed texture information about the scene in the *DoLP* and *Saturation* images. Since we are interested in region features within the image, a region based weighted average scheme is used to fuse the *DoLP* and *Saturation* images. The weights are determined by the importance of polarimetric and spectral information, and in most situations they are regarded to be of the same importance.

(5) Fuse the polarimetric *Orient* image with the multispectral *Hue* component for a new *Orient* image (*NOrientI*).

There is also little detailed texture information about the scene in *Orient* and *Hue* images. The fusion strategy of *Orient* and *Hue* images is the same as that of *DoLP* and *Saturation* images in step 3.

(6) Take the *NPI*, *NDoLPI* and *NOrientI* images obtained in steps 3, 4 and 5 as the inputs of Algorithm 1 to obtain the final fused image.

In Algorithm 2, both the polarimetric and multispectral images are mapped into the HSI color space so that they can be fused conveniently. Through fusing the polarimetric *Int* image with the multispectral *Intensity* component, the object detailed texture information from the two information sources can be well preserved. On the other hand, by fusing the polarimetric *DoLP* and *Orient* image with the multispectral *Saturation* and *Hue* components, the spectral difference and polarimetric difference information is preserved. Therefore, by integrating the spectral information into the polarimetric images, the disturbance of natural background in the polarimetric images can be reduced. Fig. 7 shows the fusion result of the scene in Fig. 3 by fusing multispectral and polarimetric imagery using the proposed Algorithm 2. The manmade objects are represented in blue color and the natural background is represented in green color. In Fig. 5(b) we have seen that by exploiting only the polarimetric information, part of the car and part of the concrete road are mistakenly regarded as the natural background. In Fig. 7, the classification is improved a lot by exploiting both the multispectral and polarimetric information.

4. Experimental results

With the algorithms presented in Section 3, a good separation of manmade objects from natural background, or metals from dielectrics, can be obtained, especially in the region of highlight areas. In this section, experiments on real images are performed to testify the proposed method.

4.1. Imaging system and data acquisition

The optical setup of the polarization and multispectral imaging system in this study is shown in Fig. 8. A non-polarization beam splitter (BS) splits the incident beam into two parts: one is used for multispectral measurements and the other is used for polarimetric measurements. In the first part, the light is filtered by a
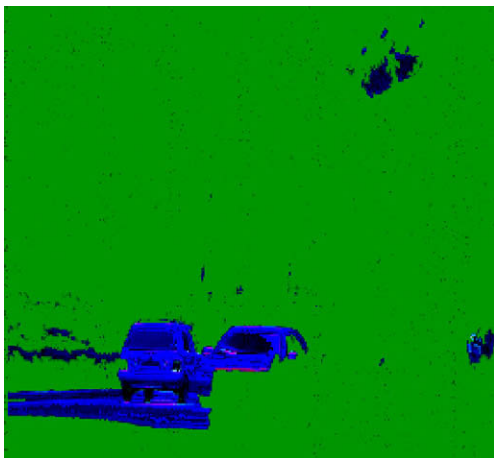
spectral filter wheel (FW) with six narrow band filters, whose central wavelengths are 404, 504, 648, 780, 880 and 1062 nm, to make it cover from visual band to near-infrared band. In the second part, the incident light is filtered by a polarimetric filter wheel (PW) with four polarizers, whose azimuth angles are set at 0°, 45°, 90° and 135°, respectively. The measurements are acquired by a standard black-and-white CCD camera. Finally, multispectral and polarimetric images are obtained simultaneously by mechanically rotating SW and PW which are controlled by a computer.

Four representative scenes are captured by using the constructed polarimetric and multispectral imaging system: two outdoor scenes and two indoor scenes. As we will see next, the proposed method gives better object separation result than the existing method.

4.2. Experiments

In this section, we use four experiments to verify the performance of the proposed method. The first two experiments are on outdoor scenes and the manmade objects are to be separated from the natural background. The last two experiments are on indoor scenes and the metal materials are to be separated from the dielectric materials. In the fourth experiment, the ground-truth segmentation was manually labeled so that the object separation accuracy can be quantitatively measured for performance evaluation.

To the best of the authors' knowledge, no polarimetric and multispectral imagery fusion method has been proposed before. Actually, few object separation methods have been proposed based on even polarimetric image fusion, among which the I_{max}/I_{min} method proposed by Wolff and Mancini [11] is commonly used and hence it is employed in the comparison.

Fig. 9(a) and (b) shows the multispectral and polarimetric intensity images of an outdoor scene, which contains objects such as car, pillar, concrete road, shrub and tree. Based on the Fresnel theory [15], polarization can reflect the object's surface characteristics and rough surface and smooth surface will have different polarimetric features. In this scene, the set of manmade objects contains car, pillar and concrete, and the reflectance is mainly composed of specular components; while the set of natural background contains shrub and tree, and the reflectance is mainly composed of diffuse components. Fig. 9(d) shows the false color polarimetry of this scene. We see that the polarimetry could give a rough separation of the scene; however, there are many separation errors. Meanwhile, the multispectral imagery could provide additional information for object separation based on the different spectral signatures of different materials. Fig. 9(c) shows the false color spectral imagery of this scene. It is expected that more accurate object separation results can be obtained by fusing the polarimetric and multispectral imagery.

Fig. 10 shows the output image by using the I_{max}/I_{min} method. We can see that it is difficult to distinguish the manmade objects,
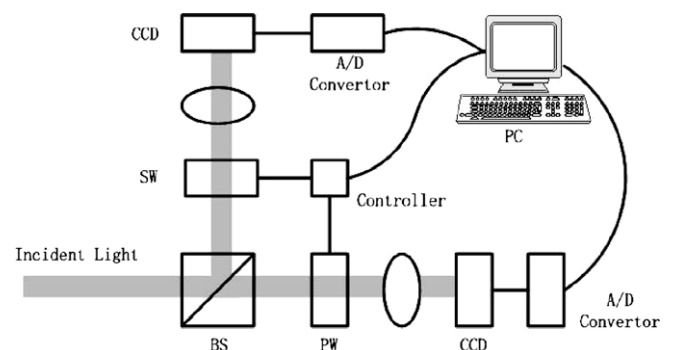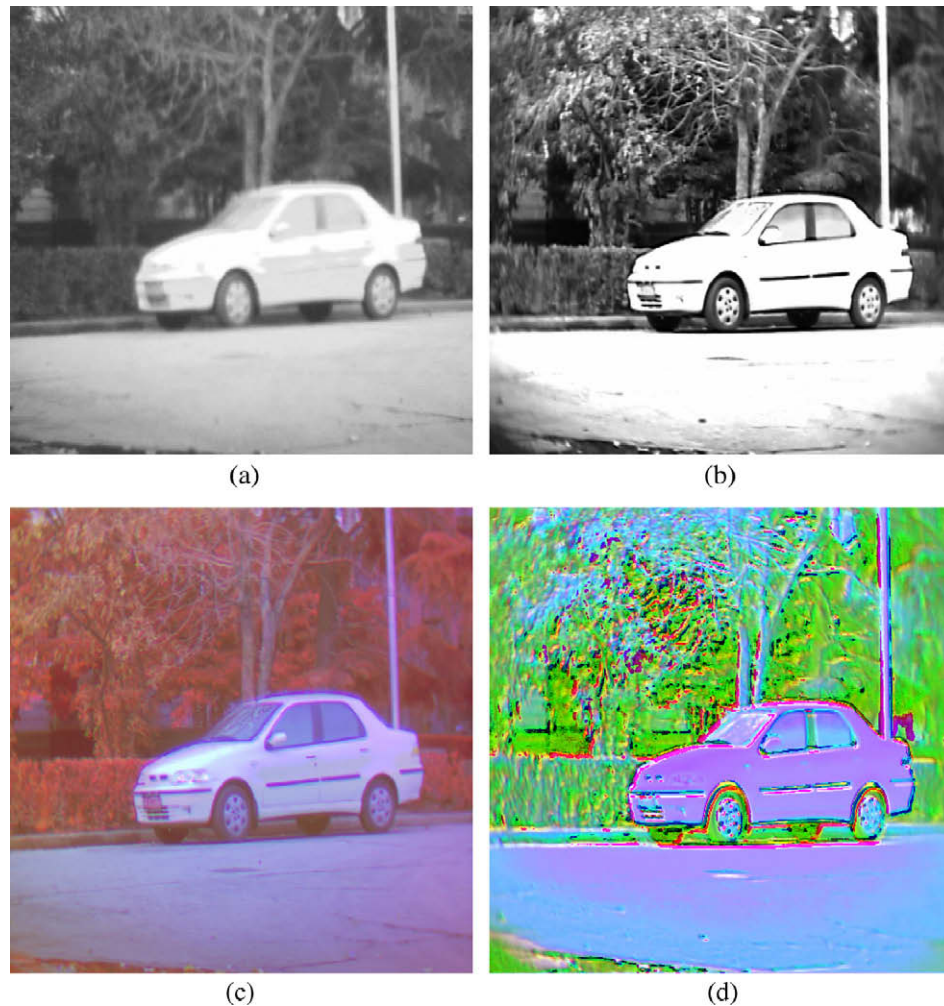

Fig. 7. The polarimetric and multispectral imagery fusion result by using the proposed Algorithm 2. Manmade objects are represented in blue color and natural background is represented in green color. (For interpretation of the references to color in this figure legend, the reader is referred to the web version of this article.)

Fig. 8. Schematic of the multispectral and polarimetric imaging system.

Fig. 9. (a) Multispectral intensity image (404, 631 and 1062 nm) and (b) polarimetric intensity image at panchromatic band of an outdoor scene; (c) multispectral false color image (R is the image at 1062 nm, G is the image at 631 nm and B is the image at 404 nm); (d) polarimetric false color image (R is the intensity image, G is the DoLP image and B is the *Orient* image). (For interpretation of the references to color in this figure legend, the reader is referred to the web version of this article.)
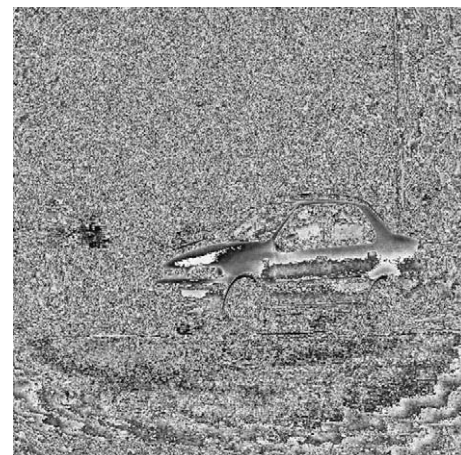
except for part of the car and part of the pillar, from the natural background. The concrete road, automobile chassis and most of the pillar are merged into the background of tree and shrubs. Under different thresholds, the manmade and natural objects cannot be distinguished in Fig. 10.

Fig. 11(a) shows the polarimetric imagery fusion result by combining *Int*, *DoLP* and *Orient* images using the proposed Algorithm 1. Fig. 11(b) shows the fusion result by integrating multispectral and polarimetric imagery using the proposed Algorithm 2. In Fig. 11, manmade object is represented in red color and natural background is represented in blue color. We can see from Fig. 11(a) that by exploiting only the polarimetric information, part of the tree and shrubs is mistakenly classified as manmade objects. The classification is improved a lot by exploiting both the multispectral and polarimetric information in Fig. 11(b).

Fig. 12 shows the intensity image of another outdoor scene, which contains five airplane models (highlighted by the red circle) in the grass land. Fig. 13 shows the output image by using the I_{max}/I_{min} method. Obviously, it is hard to distinguish the airplane models from grass land in Fig. 13. Fig. 14 shows the fusion results by the proposed Algorithm 1 and Algorithm 2. In Fig. 14, manmade object is represented in red color and natural background is represented in black and green color. We can see from Fig. 14(a) that by exploiting only the polarimetric information, the manmade airplane models and a large part of the grass land cannot be well
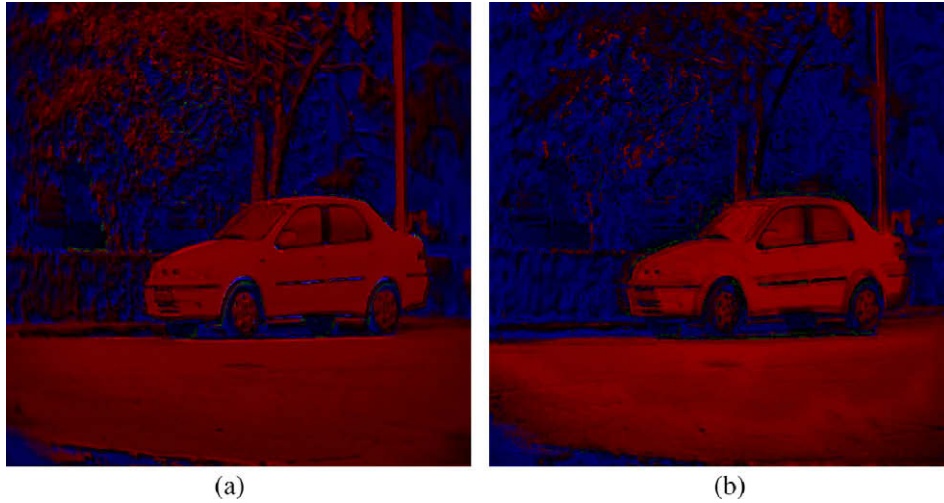
distinguished. However, by using the proposed Algorithm 2 to exploit both multispectral and polarimetric information, the five airplane models can be clearly identified in Fig. 14(b).

The previous two experiments illustrate that the proposed method is effective to separate manmade objects from natural

Fig. 10. The image by I_{max}/I_{min}.

Fig. 11. (a) The polarimetric imagery fusion result by using the proposed Algorithm 1; (b) the polarimetric and multispectral imagery fusion result by using the proposed Algorithm 2. Manmade object is represented in red color and natural background is represented in blue color. (For interpretation of the references to color in this figure legend, the reader is referred to the web version of this article.)
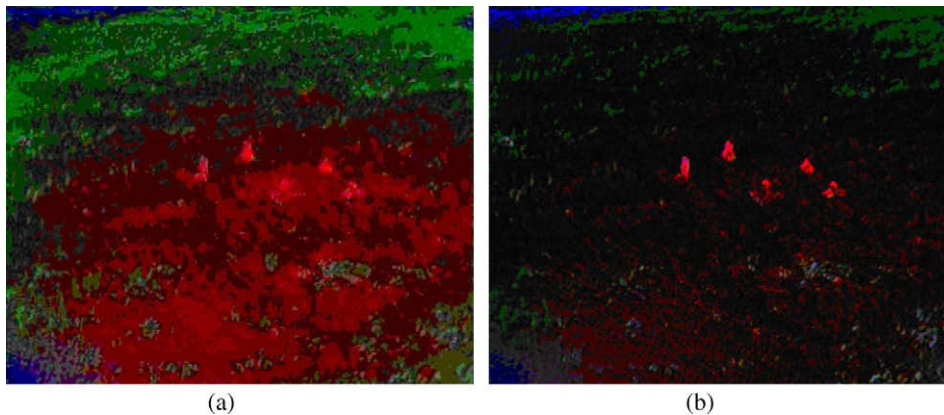

Fig. 12. Intensity image of an outdoor scene.

Fig. 13. The image by I_{max}/I_{min}.

background. Next, let us test its performance in distinguishing different materials. Fig. 15 shows an indoor scene of circuit board. There are three basic types of material regions, solder copper lead, soldering tin and plastic dielectric in the circuit board, which is illuminated under the standard fluorescent ceiling lighting. Fig. 16 shows the I_{max}/I_{min} image, from which we can see that on the top part of circuit board the plastic and solder copper are difficult to be distinguished from each other.

Fig. 17(a) is shown in blue and purple colors, where blue corresponds to soldering tin, purple correspond to solder copper lead and plastic dielectric. As the difference of solder copper lead and plastic dielectric is very small, their color difference is very small. Fig. 17(b) is shown in blue, yellow and red colors, where blue corresponds to soldering tin, yellow corresponds to solder copper lead, and red corresponds to plastic dielectric. Comparing Fig. 17(a) with (b), we can clearly see that better dielectric/metal

Fig. 14. (a) The polarimetric imagery fusion result by using the proposed Algorithm 1; (b) the polarimetric and multispectral imagery fusion result by using the proposed Algorithm 2.
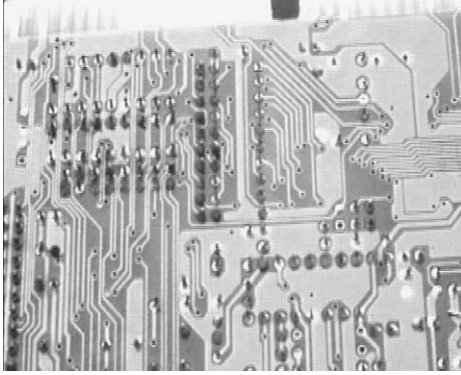
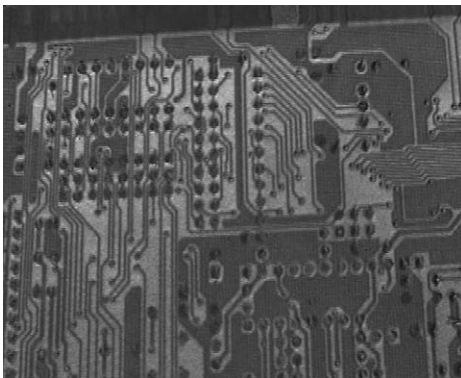**Fig. 15.** Intensity image of a circuit board.

Fig. 16. The image by I_{max}/I_{min}.

material identification result on circuit boards can be obtained through fusing spectral and polarimetric imagery than just using polarimetric or spectral imagery.

To quantitatively evaluate the object separation performance of the proposed algorithm, we made the following experiment. Fig. 18(a) shows an indoor scene (in tent), where there are five plates with different shapes and sizes in the grassland. These plates are all metals and the scene is illuminated under the standard fluorescent ceiling lighting. The ground-truth segmentation of the plates is labeled manually, which is shown in Fig. 18(b). Fig. 18(c) shows the I_{max}/I_{min} image, and Fig. 18(d) shows the polarimetric and multispectral imagery fusion result by using the proposed Algorithm 2, where red color represents the metal plates

and blue color represents the grassland. Through subtracting the ground-truth from the segmentation results, the separation errors by using I_{max}/I_{min} and Algorithm 2 are shown in Fig. 18(e) and (f), respectively. It can be seen that the proposed Algorithm 2 achieves much better object separation results than can I_{max}/I_{min}.

To quantitatively evaluate the separation performance, we employ the overall accuracy (OA) [26] to measure the separation accuracy of the whole scene, and employ the kappa coefficient [26] to measure the correspondence of the separation with two categories – metal object and grass background. The OA coefficient is the percentage of correctly classified pixels, which is defined as

$$OA = \frac{N_C}{N_T}, \tag{16}$$

where N_T is total number of pixels and N_C is the number of correctly classified pixels.

The kappa coefficient is a statistical measure of the agreement between the map of segmentation result and the map of ground-truth, which is defined as

$$K = \frac{L\sum_{j=1}^{J} x_{jj} - \sum_{j=1}^{J} x_{j+}x_{+j}}{L^2 - \sum_{j=1}^{J} x_{j+}x_{+j}}, \tag{17}$$

where J is the number of rows in the confusion matrix, x_{jj} is the element of confusion matrix in the jth row and the jth column, x_{j+} is the sum of the jth row in confusion matrix, x_{+j} is the sum of the jth column in confusion matrix, and L is the sum of all elements in the matrix. For more information about the kappa coefficients, please refer to [26]. The kappa coefficients of the two categories are denoted as K-m (for metal) and K-g (for grass), respectively. Table 1 lists the results of the OA, K-m and K-g by the two separation methods. We see that the proposed method achieves much better result than the I_{max}/I_{min} method.

From the above experiments, we can see that there are many potential applications of the proposed methods in manufacturing and quality control (e.g. the 3rd experiment), object detection and recognition (e.g. the 1st, 2nd and 4th experiments) by exploiting both the surface descriptions and material composition descriptions of the objects using spectral-polarimetric imaging. It cannot only improve much the classification accuracy of metals from dielectrics, but also improve the detection accuracy of manmade objects from natural background.

5. Conclusion

In this paper, a DoLP modulation based polarimetric imagery fusion method was first developed to separate the manmade
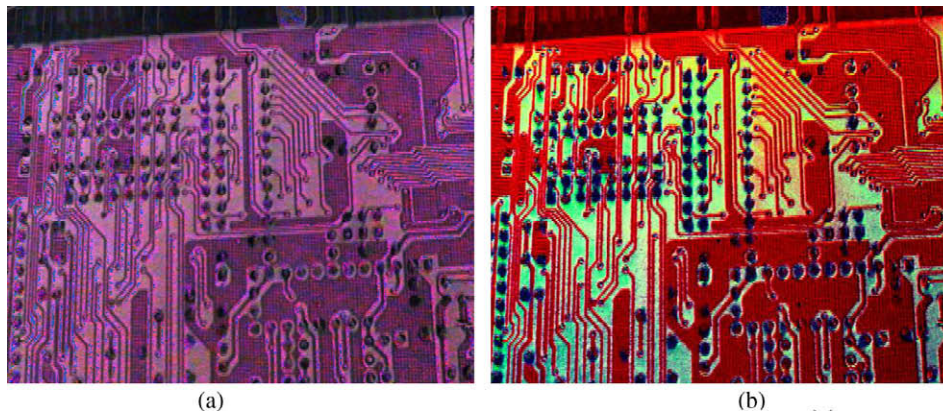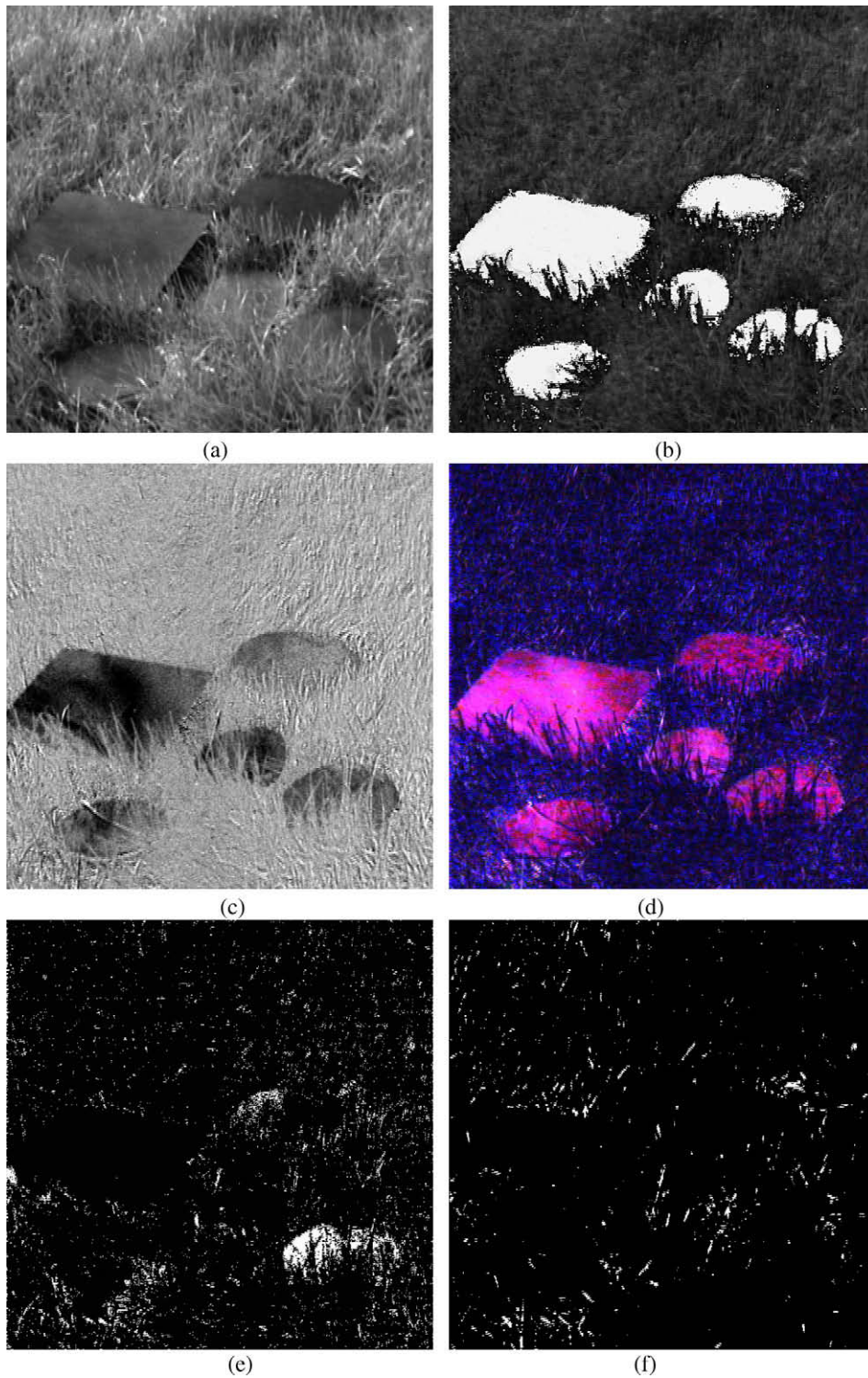

(a)

(b)

Fig. 17. (a) The polarimetric imagery fusion result by using the proposed Algorithm 1; (b) the polarimetric and multispectral imagery fusion result by using the proposed Algorithm 2.

Fig. 18. (a) Intensity image; (b) manually labeled ground-truth; (c) the image by I_{max}/I_{min}; (d) the polarimetric and multispectral imagery fusion result by using the proposed Algorithm 2; (e) separation errors by using the I_{max}/I_{min}; (f) separation errors by using the proposed Algorithm 2.

objects from the natural background based on the different characteristics of their surfaces. Then a novel spectral and polarimetric imagery fusion method was proposed for better separation results through fusing the spectral and polarimetric information provided by the specular and diffuse reflected light. Experiments on real outdoor and indoor scenes were conducted to verify the performance of the proposed algorithms. The proposed methods are simple yet powerful, and completely passive, requiring only the sensing of

transmitted radiance of reflected light through a polarizing filter positioned in multiple orientations, and narrow band band-pass

Table 1
Separation results by different methods.

Methods	OA (%)	K-m (%)	K-g (%)
I_{max}/I_{min}	70.5	60.3	83.6
Proposed method	91.8	97.5	86.4

spectral filters in front of a camera. They can be applied to high-level vision tasks such as object classification and recognition and camouflage identification, etc.

References

[1] S. Umeyama, G. Godin, Separation of diffuse and specular components of surface reflection by use of polarization and statistical analysis of images, IEEE Transactions on Pattern Analysis and Machine Intelligence 26 (5) (2004) 639–647.

[2] G.A. Atkinson, E.R. Hancock, Recovery of surface orientation from diffuse polarization, IEEE Transaction on Image Processing 15 (6) (2006) 1653–1664.

[3] L.B. Wolff, T.E. Boult, Constraining object features using a polarization reflectance model, IEEE Transactions on Pattern Analysis and Machine Intelligence 13 (7) (1991) 635–657.

[4] G.A. Atkinson, E.R. Hancock, Robust estimation of reflectance functions from polarization, Lecture Notes in Computer Science 4478 (2007) 363–371.

[5] Y.Y. Schechner, N. Karpel, Clear underwater vision, in: Proceedings of the 2004 IEEE Computer Society Conference on Computer Vision and Pattern Recognition, vol. 1, 2004, pp. 536–543.

[6] L.B. Wolff, Polarization-based material classification from specular reflection, IEEE Transactions on Pattern Analysis and Machine Intelligence 12 (11) (1990) 1059–1071.

[7] S.H. Sposato, Matthew P. Fetrow, Two long-wave infrared spectral polarimeters for use in understanding polarization phenomenology, Optical Engineering 41 (5) (2002) 1055–1064.

[8] H. Chen, L.B. Wolff, Polarization phase-based method for material classification and object recognition in computer vision, CVPR (1996) 128–135.

[9] A. Filippidis, L.C. Jain, N.M. Martin, Using genetic algorithm and neural networks for surface land mine detection, IEEE Transaction on Signal Processing 47 (1) (2001) 176–186.

[10] G.A. Shaw, H.K. Burke, Spectral imaging for remote sensing, Lincoln Laboratory Journal 14 (1) (2003) 3–28.

[11] L.B. Wolff, T.A. Mancini, Philippe Poluiquen, et al., Liquid crystal polarization camera, IEEE Transactions on Robotics and Automation 13 (2) (1997) 195–203.

[12] S.K. Nayar, K. Ikeuchi, T. Kanade, Surface reflection: physical and geometrical perspectives, IEEE Transactions on Pattern Analysis and Machine Intelligence 13 (7) (1991) 611–634.

[13] Y. Zhao, Q. Pan, H. Zhang, Material classification based on multi-band polarimetric images fusion, polarization: measurement, Analysis, and Remote Sensing VII 6240 (2006) 71–77.

[14] H. Chen, L.B. Wolff, Polarization phase-based method for material classification in computer vision, International Journal of Computer Vision 28 (1) (1998) 73–83.

[15] D. Goldstein, Polarized Light, second ed., Marcel Dekker, New York, 2003, pp. 31–63 (Chapter 4), pp. 133–145 (Chapter 8)..

[16] R. Siegal, J.R. Howell, Thermal Radiation Heat Transfer, second ed., Springer, Berlin, 1981. pp. 93–133 (Chapter 4).

[17] A. Plaza, P. Martinez, R. Perez, et al., A new approach to mixed pixel classification of hyperspectral imagery based on extended morphological profiles, Pattern Recognition 37 (6) (2004) 1097–1116.

[18] C.E. Shannon, A mathematical theory of communication, The Bell System Technical Journal 27 (7) (1948) 379–423.

[19] A. Toet, J. Walraven, New false colour mapping for image fusion, Optical Engineering 35 (3) (1998) 650–658.

[20] J.R. Schott, Remote Sensing: The Image Chain Approach, Cambridge University Press, New York, 2007, pp. 13–17 (Chapter 1).

[21] J.J. Lewis, Robert J. O_Callaghan, Stavri G. Nikolov, et al., Pixel and region-based image fusion with complex wavelets, Information Fusion 2 (2005) 19–130.

[22] Y. Zhao, Q. Pan, H. Zhang, New polarization imaging method based on spatially adaptive wavelet image fusion, Optical Engineering 4 (12) (2006) 123–202.

[23] G. Pajares, J.M. Cruz, A wavelet-based image fusion tutorial, Pattern Recognition 37 (9) (2004) 1855–1872.

[24] S. Tominaga, S. Okamoto, Reflectance-based material classification for printed circuit boards, in: Proceedings of the 12th International Conference on Image Analysis and Processing (ICIAP'03), 2003, pp. 17–19.

[25] G. Piella, A general framework for multiresolution image fusion: from pixels to regions, Information Fusion (4) (2003) 259–280.

[26] J.L. Fleiss, J. Cohen, B.S. Everitt, Large sample standard errors of kappa and weighted kappa, Psychological Bulletin 72 (5) (1969) 323–327.